ELSEVIER

Journal of Fluids and Structures 22 (2006) 21–43

JOURNAL OF FLUIDS AND STRUCTURES

www.elsevier.com/locate/jfs

Drag measurement and dynamic simulation of Martian wind-driven sensor platform concepts

S.E. Rose, C.B. Moody, D.L. James, A.A. Barhorst*

Texas Tech University, Department of Mechanical Engineering, Lubbock, TX 79409-1021, USA

Received 11 December 2004; accepted 4 September 2005
Available online 25 October 2005

Abstract

The purpose of this work is to (a) determine the drag coefficient of three wind-driven systems (referred to as tumbleweeds) in a simulated Martian atmospheric boundary layer; two concepts from NASA Langley (LaRC) and one from Texas Tech University (TTU), and (b) perform a dynamic analysis of the TTU tumbleweed to establish the feasibility of operation in a simulated Martian environment. The TTU Wind Tunnel is used in order to determine the drag coefficient for the tumbleweeds in both the aerodynamic and atmospheric boundary layer (ABL) test sections. A comparison of the two mean drag coefficients for each tumbleweed model reveals the extent to which an ABL affects drag on the models. It appears that no transformation exists that can be used to transform aerodynamic-based drag coefficients into boundary-layer-based drag coefficients; therefore, reliance upon ABL tests is important. It is generally accepted that a complete ABL test under conditions of neutral atmospheric stability requires knowledge of the incoming (approach) mean velocity and turbulent intensity profile, spectral distribution, roughness height, and Reynolds number. Given the fact that limited data exists for the Martian flows, physical simulations of an atmospheric surface layer with knowledge of the mean velocity and general turbulence characteristics was developed in order to obtain drag coefficients for several tumbleweed wind platform designs. The tumbleweeds drag coefficients were effectively constant with the boundary layer affected coefficient less than the respective aerodynamically obtained coefficient. Of particular interest in this study is the TTU tumbleweed, which underwent extensive testing in order to obtain a force function to describe its aerodynamic characteristics in any orientation relative to the wind.

Keywords: Mars; Tumbleweed; Wind-driven rovers; Coefficient of drag measurement; Wind tunnel; Atmospheric boundary layer; Fluid-structure interaction; Simulation; Rolling dynamics

1. Introduction

Martian surface exploration has moved from science-fiction to reality in the past few decades. With several successful missions, such as the Mars Global Surveyor, Mars Odyssey, and the Spirit and Opportunity rovers, a knowledge base about the surface conditions on the planet is being developed. The first missions aimed at Mars exploration, starting in 1964, were so-called "fly by" missions, where Mariners 3–4 and Mariners 6–7 simply took pictures of the planet as they passed by. The missions quickly progressed into orbiters, in 1971, with Mariner 9 being the first satellite to orbit Mars,

*Corresponding author. Tel.: +1 806 742 3563 X 241.
E-mail address: alan.barhorst@ttu.edu (A.A. Barhorst).

0889-9746/$ - see front matter © 2005 Elsevier Ltd. All rights reserved.
doi:10.1016/j.jfluidstructs.2005.09.008

Nomenclature

A	frontal area
$\hat{b}_i$	right-handed unit vector triad defining the body reference frame ($i = 1, 2, 3$)
C_D	drag coefficient
C_{rr}	coefficient of rolling resistance
F_D	drag force
F_g	gravitational body forces
F_{rr}	rolling resistance force
g	gravitational acceleration
I_i	turbulence intensity in the i-direction ($i = u, v, w$), S_i/U where S_i is the standard deviation of the ith component of velocity and U is the mean velocity
Je	Jensen number, l_c/z_o
l_c	a characteristic length; choice depends on situation, e.g., model height or roughness length
m	tumbleweed mass
$\hat{n}_i$	right-handed unit vector triad defining the Newtonian reference frame ($i = 1, 2, 3$)
q_i	generalized coordinate ($i = 1, 2, 3, 4, 5$)
$\dot{q}_i$	generalized speed ($i = 1, 2, 3, 4, 5$)
R	model radius
Re_D	Reynolds number, $U_{\mathrm{ref}} l_c/\nu$
r_{model}	model radius
t	plate thickness
U_{ref}	reference velocity (at model height for ABL simulations, mid-height for the aerodynamic simulations)
${}^{o}\vec{v}^{\mathrm{cg}}$	velocity of the center of gravity of the tumbleweed with respect to the origin
$\vec{V}_{\mathrm{rel}}$	relative velocity between the wind velocity and tumbleweed velocity
V_{wind}	wind velocity vector
z_{cg}	height of the center of gravity of the test models in the wind tunnel
z_o	aerodynamic roughness height
${}^{N}\vec{\alpha}^{B}$	angular acceleration of the body frame as seen from the Newtonian frame
θ	angle of inclination
ρ	density
${}^{N}\vec{\omega}^{B}$	angular velocity of the body frame as seen from the Newtonian frame

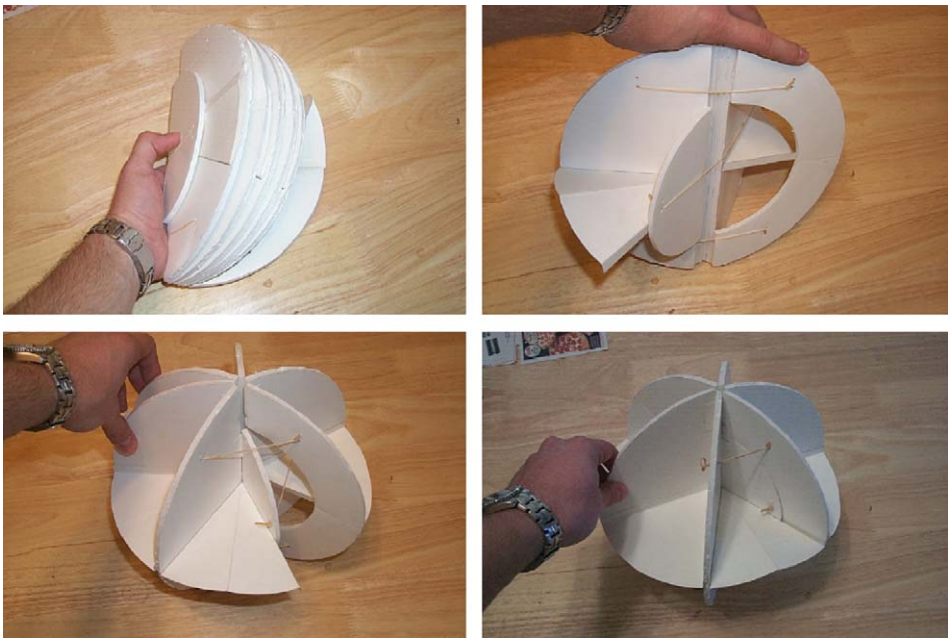

Fig. 1. Tumbleweed concept deployment.

and landers, in 1975, with Vikings 1 and 2 being the first to land on the planet (NASA, 2004). These missions along with a number of other orbiters and landers have provided researchers with a vast amount of information about the "Red Planet."

There are many areas of ongoing research for future exploration vehicles designed with varying surface exploration tasks in mind. The most common factors among virtually all of the landers that have been placed on the Martian

surface is their limited range of exploration, and high cost and complexity. The concept under investigation herein is a completely different approach to exploring the surface of Mars. The concept is a low cost, wind-driven sensor platform that is intended to be used as a means of taking surface composition data over most of the surface of the planet that will be referred to as a tumbleweed (both Texas Tech University (TTU) and NASA Langley (LaRC) have wind-driven platforms that are called tumbleweeds). Large coverage areas are to be achieved through placing thousands of these devices on the surface and allowing them to travel freely with the wind. One of the most important characteristics of this concept is its collapsible design, shown in Fig. 1, that allows for the transportation of large numbers of the devices in the very limited space available on current transport vehicles.

The collapsible design shown in the above figure was developed from the similar paper party-ball collapsing design. The geometry of the tumbleweed concept is that of a sector-removed sphere, having many corners for radar reflectivity and ample surface area for sensors, solar cells, and wind reflection. It is also thought that the device can be constructed from inexpensive materials such as paper goods or much lighter material such as the forthcoming polymer fabrics with embedded organic circuitry. Using an inexpensive, collapsible, sensor platform such as this allows for a wide variety of sensors to be placed on the surface of the planet with redundancy in numbers and a passive transportation mechanism.

2. Wind tunnel testing

2.1. Test set-up and facility

The wind tunnel facility in the Mechanical Engineering Department at TTU is somewhat unique in its capabilities. It contains two distinct test-sections, one for classic aerodynamic testing and a second for atmospheric boundary layer (ABL) testing. The wind tunnel, shown schematically in Fig. 2, is powered by a 250 HP fan that is capable of producing roughly 50 m/s winds at the test sections. As the flow travels around the 180° bend just before the contraction, vortices are first reduced by a honeycomb structure and then straightened further with a set of fine mesh screens to provide a highly uniform flow in the aerodynamic test section. Just beyond the aerodynamic test-section, there is a 15.2 m section where various roughness elements can be placed to generate numerous boundary layer profiles that can be tuned to the test requirements. These roughness elements consist of everything from carpet to bricks on the floor and are typically accompanied by a fence barrier placed at the downstream side of the aerodynamic test-section. The fence barrier creates an initial momentum deficit in the lower region of the flow and is typically used to establish the boundary layer height. The floor roughness elements are used to simulate different terrain roughness, and can change the roughness height, z_o, values for the flow.

The wind tunnel test set-up was constructed as shown in Fig. 3. A base plate bolted to the wind tunnel floor holds the upright beam and allows for the height of the setup to be adjusted according to test requirements. A mounting adapter for the force/torque (F/T) sensor fits directly into the upright beam and accepts the sensor on the opposing end. Another mounting adapter is mounted directly on the face of the sensor and accepts the model on its opposing side.

2.1.1. Test models

A total of five different wind tunnel test models were constructed and tested in this study, three from TTU and two from LaRC, see Fig. 4. The sphere and flat plate models were tested for assumption verification, as will be discussed later. The models were sized to have a test range for Reynolds numbers in the range of $10^5 \leqslant \mathrm{Re}_D \leqslant 10^6$. In addition, the TTU tumbleweed, 0.3 m in diameter, was fitted with a custom-made ball joint in order to mount the model in various ranges of pitch, yaw, and roll orientation angles. The ball joint mount allows for orientation angle ranges of pitch 0–30°, yaw 0–30°, and roll 0–34°. The top and bottom of the TTU configuration looks like a flat plate to the oncoming wind which allowed the mean drag, hereafter referred to solely as drag, in those orientations to be taken as that of a flat plate in cross-flow. Combining this with the symmetry of the tumbleweed provides a significant data coverage area.

2.1.2. Experimental uncertainties

The uncertainty in the drag measurement was calculated based on the uncertainties in the drag force measurement, atmospheric density, and mean velocity using the root-mean-square method of Kline and McClintock (1953). The uncertainty in the atmospheric density is neglected due to very little or no change in the pressure and temperature during each test. The force/torque sensor was calibrated statically with a resulting uncertainty that matched the manufactured specification of $\pm 0.05\%$ full scale. The uncertainty in the velocity probe was ± 0.4 m/s and was the largest contributor to the overall uncertainty in drag. The percent uncertainty in drag measurement is shown in Fig. 5, where it is seen that the value of uncertainty in the drag measurement is large at low wind speeds and decreases to less

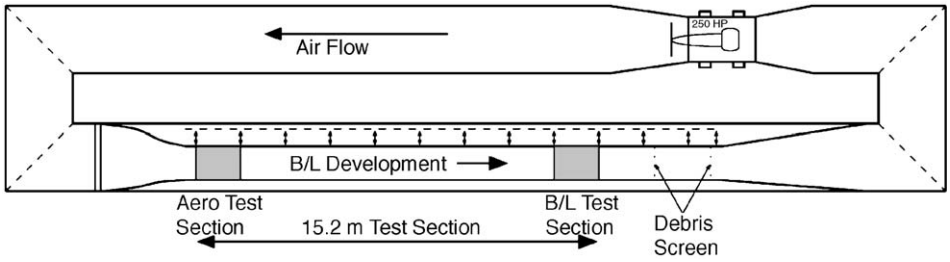

Fig. 2. Texas Tech wind tunnel.

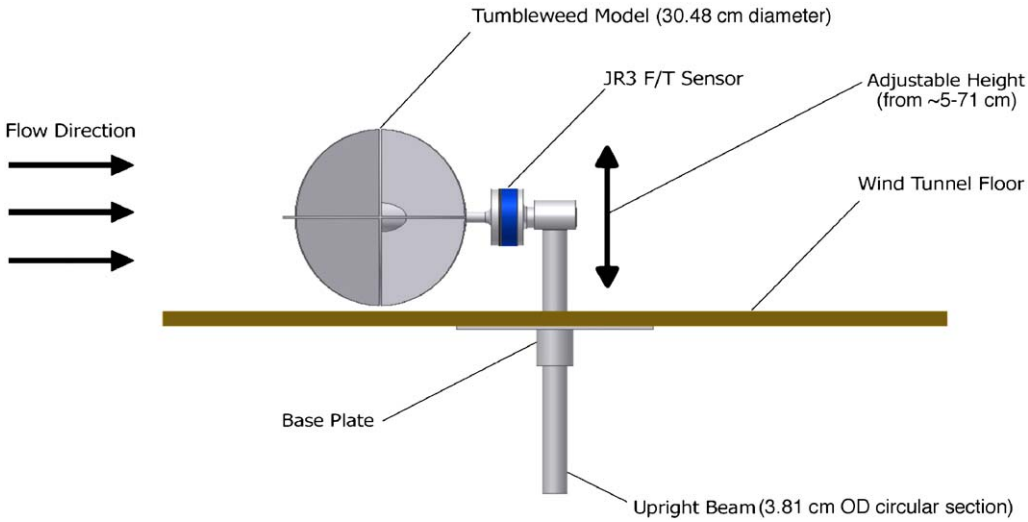

Fig. 3. Wind tunnel test set-up.

than 10% at wind speeds greater than 20 m/s. This was due to the large relative uncertainty in the velocity measurement at low wind speeds, because the uncertainty in the drag coefficient is most influenced by the uncertainty in velocity, thus necessitating the need to show Reynolds number independence; the relative uncertainty decreases as the velocity increases. A more sensitive sting/load cell combined unit was initially utilized as well, but was found to be impractical because of vortex-shedding-induced resonance observed in the tumbleweed/support structure system. Therefore, we utilized a stiff support structure with a less sensitive load cell while testing at higher wind speeds.

2.2. Drag-orientation analysis

In order to obtain the drag-orientation data required for the dynamic model, force data for roughly 90 different orientations was needed. To obtain a measurement of the angle of rotation of the tumbleweed model, two laser pointers were fixed to the model, one pointing vertically and one pointing horizontally. These lasers would then create points on the wall and ceiling of the wind tunnel that would correspond to a set of (pitch, yaw, roll) angles. Using vector algebra, the orientation angles were then determined from the locations of the laser points on the wall and ceiling of the wind tunnel. The equations were overdetermined so they were solved in a least-squares sense.

3. Wind tunnel results

In testing objects in a simulated neutral ABL and neglecting the Coriolis acceleration, one usually scales the velocity profile to match a desired full-scale velocity profile through the matching of the appropriate nondimensional terms. The Reynolds number is evaluated to ensure that the flow is fully turbulent and velocity traverses are taken to ensure that

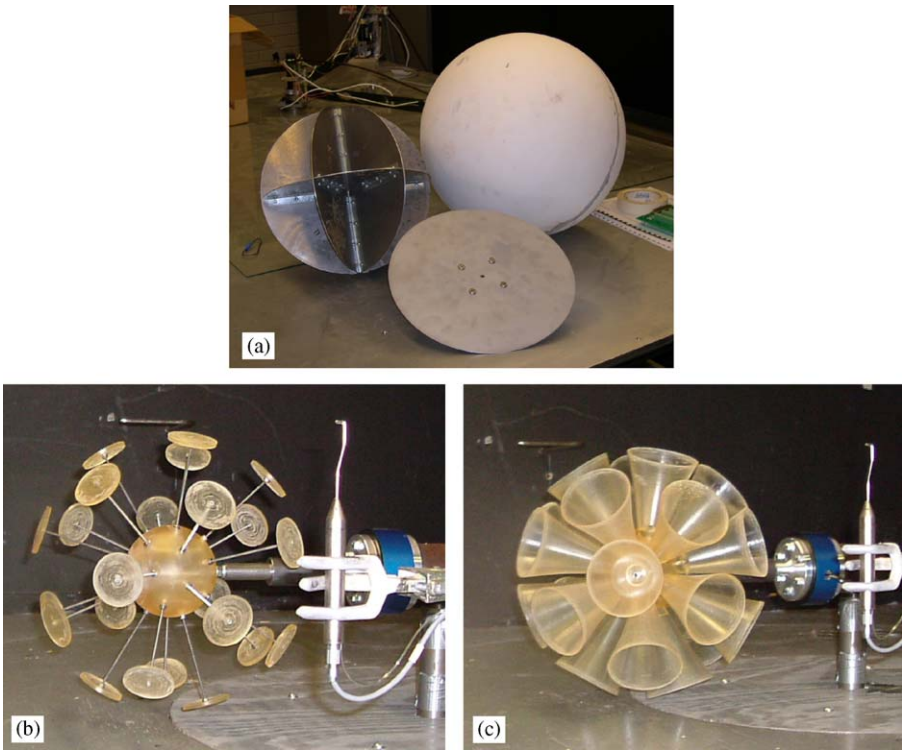

Fig. 4. Wind tunnel test models: (a) TTU tumbleweed and verification models; (b) LaRC dandelion model; (c) LaRC tumblecup model.

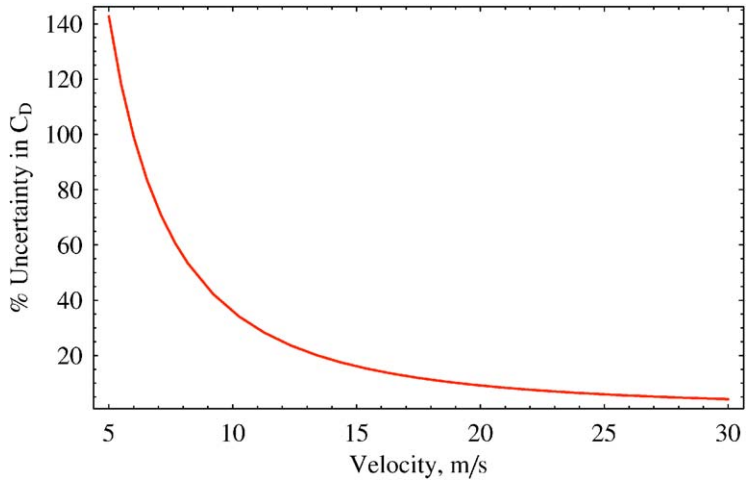

Fig. 5. Drag measurement uncertainty as a function of wind velocity.

the boundary layer fully engulfs the model. Little data for the turbulence spectra on Mars is available, and only a mean horizontal velocity distribution written in terms of the traditional log-law is known (Justus and Johnson, 2001); therefore, only the mean profile, friction velocity, and roughness height can be matched. Scaling of the Reynolds and Jensen numbers would require the velocity at the model height to be tested in the TTU tunnel at velocities between 1 and 1.7 m/s. Obtaining drag measurements with the F/T sensor at these speeds results in data that is within the uncertainty of the F/T sensor.

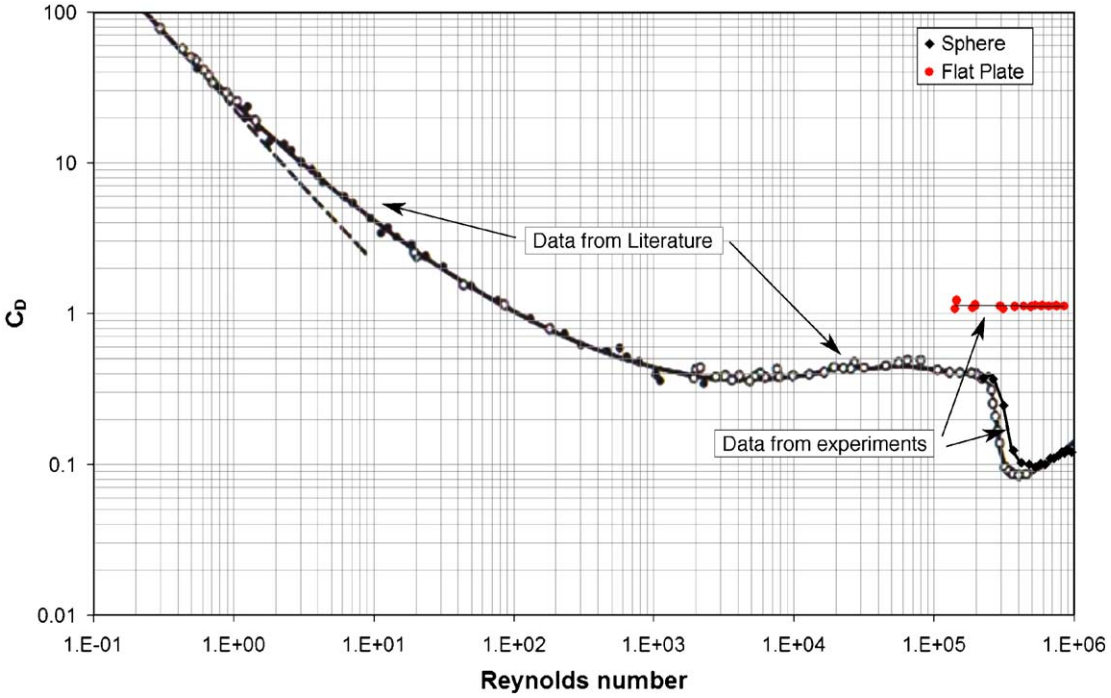

Fig. 6. Wind tunnel verification results.

Upon inspection of the LaRC and TTU tumbleweed models, it was hypothesized that the sharp edges of the models would lead to separation that is essentially independent of Reynolds number, much like sharp-edged buildings. If this is true, it allows the tumbleweed to be tested in specific ABL velocity profiles that greatly increase the accuracy of the results. The immediate goal of the wind tunnel testing is to determine the drag coefficient for the various tumbleweeds in a simulated ABL and compare those results with drag coefficients obtained from a uniform (aerodynamic) flow to be able to determine what, if any, differences existed. The drag coefficients determined in the ABL will be used in a dynamic analysis that predicts the TTU tumbleweed motion, see Section 4.

To verify the assumption of drag independent Reynolds number and the accuracy of the test setup, a sphere and a flat plate models were tested and compared to results found in Schlichting (1979). These two geometries were chosen because their drag characteristics have been well documented in the literature. The drag coefficient of a sphere is known to be Reynolds number dependent, having a pronounced change in C_D in the transition region from laminar to turbulent flow. The flat plate is known to maintain a constant C_D through a wide range of Reynolds numbers, including the range tested in this work. It was found that the set-up provided very accurate results with both the sphere and flat plate as shown in Fig. 6. The curve in the figure was taken from Schlichting (1979). The experimental data from this work was then overlayed on the curve as seen in the figure. The results from the flat plate showed an average C_D of 1.12 compared to the published value of 1.17, a 4.3% difference.

3.1. Aerodynamic results

After obtaining the setup verification results in the aerodynamic test section, the tumbleweed model was tested to determine its drag coefficient as a function of Reynolds number. As assumed, the tumbleweed drag coefficient is dominated by pressure drag as in the case of the flat plate. The LaRC models, too, show a clear independence of Reynolds number in drag. Fig. 7 shows the results from the aerodynamic testing on the flat plate, tumbleweed, and LaRC models.

3.2. Atmospheric boundary layer results

Hoerner (1965) states that the presence of a boundary layer (i.e., ground effects) has considerable influence on the pressure distribution and drag of simple bluff bodies in which the drag coefficient is reduced in comparison to free-

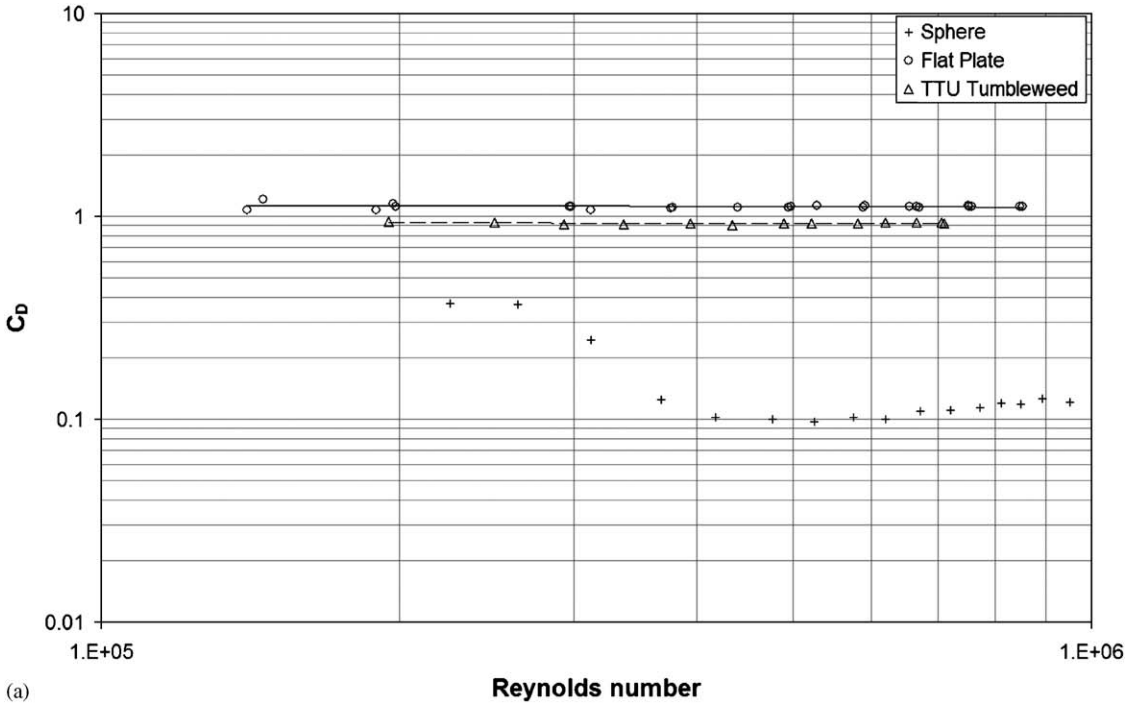

(a)

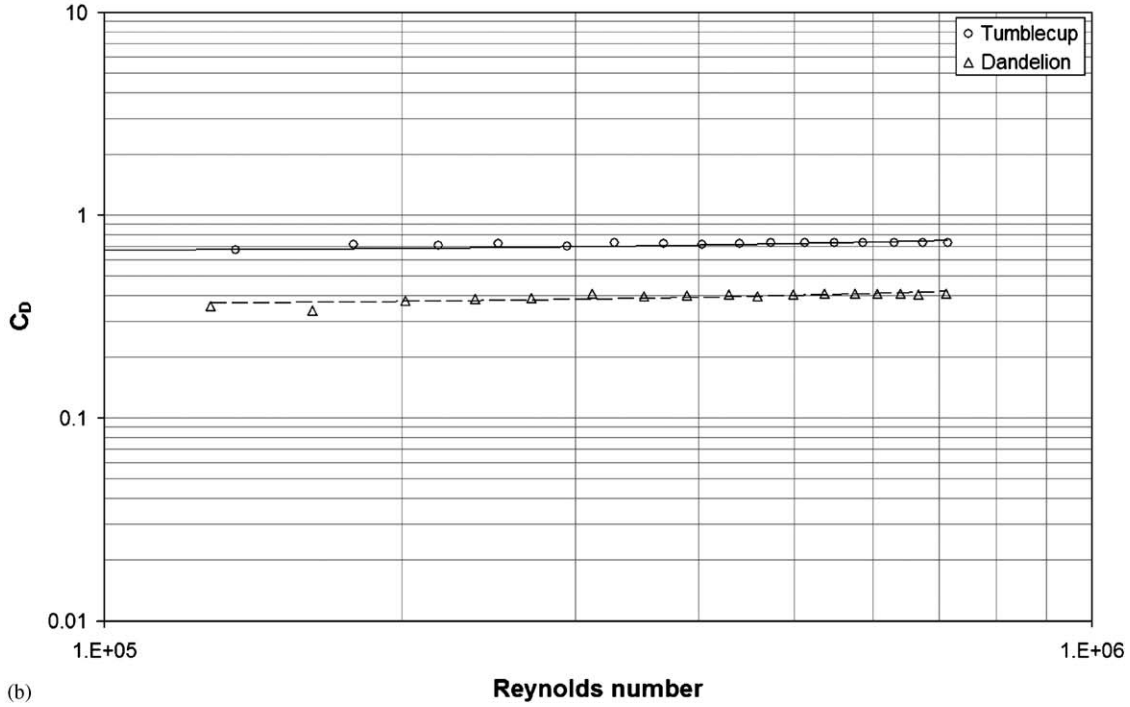

(b)

Fig. 7. C_D versus Re_D for all models: (a) TTU tumbleweed and flat plate; (b) LaRC models.

stream values. However, Hoerner also states that three-dimensional bluff bodies that are not of streamline shape are relatively unaffected by the boundary layer. More recent work on the drag of buildings in ABLs (Lee, 1976; Cheng et al., 1992; Li and Melbourne, 1995; Flay and Vickery, 1995) have demonstrated that the mean drag force for many

sharp-edged bluff bodies, not of streamline shape, are affected by the turbulent intensity and turbulence length scale. In general, as the turbulence intensity increases, the drag tends to be reduced because the turbulence interacts with the separated shear layer causing the wake to be reduced, yielding a more complete pressure recovery. Although most of these works were performed on sharp-edged building models, the sharp-edged design of the LaRC and TTU tumbleweeds are three-dimensional bluff bodies that should have fixed separation points, and therefore, might follow similar trends.

Before presenting the results of the ABL testing, the boundary layer profiles must first be presented to better understand the flow field to which the models were subjected. Boundary layer profiles were measured using a traverse mechanism with a three-axis Cobra Probe. The velocity was sampled at 1 kHz for 1 min. All measurements were taken at the center span in the boundary layer section, and the results represent the mean data flow profiles. Fig. 8 shows five different boundary layer profiles taken at different model height. As seen in the figure, the flow profile changes considerably as the mean wind speed changes. The corresponding roughness heights that were generated for the mean velocity profiles used in the tests varied two orders of magnitude, but were still smoother than would be required for Jensen scaling.

All test models were fully immersed (i.e., the boundary layer height was much greater than the height of the models) in a boundary layer profile and tested to determine drag coefficient as a function of Reynolds number to compare with the results from the aerodynamic testing. The center of gravity (CG) for each model was positioned at the center of the wind tunnel, $z_{cg}/r_{model} = 2$, for the aerodynamic tests such that each model was subjected to a uniform velocity with no boundary layer. For the ABL tests, the CG was positioned just greater than the respective radius of the model so that $z_{cg}/r_{model} \approx 1$. The results from the boundary layer testing for all five models are shown in Fig. 9. The drag coefficients of the various models showed a fairly uniform decrease between 6% and 16% when compared to the free-stream results.

In an effort to evaluate the effect of free-stream turbulence on the ABL tests, two different turbulence augmentation devices were placed at the contraction region of the wind tunnel and the tumbleweeds were tested with these set-ups. The first device is a set of spires that generate vertically oriented vortices throughout the flow and the second is a grid that produces large-scale vortices oriented in both the horizontal and vertical directions. Turbulent intensity profiles for three different boundary layer profiles generated with carpet and a 25.4 cm fence alone, with a grid, or with spires are

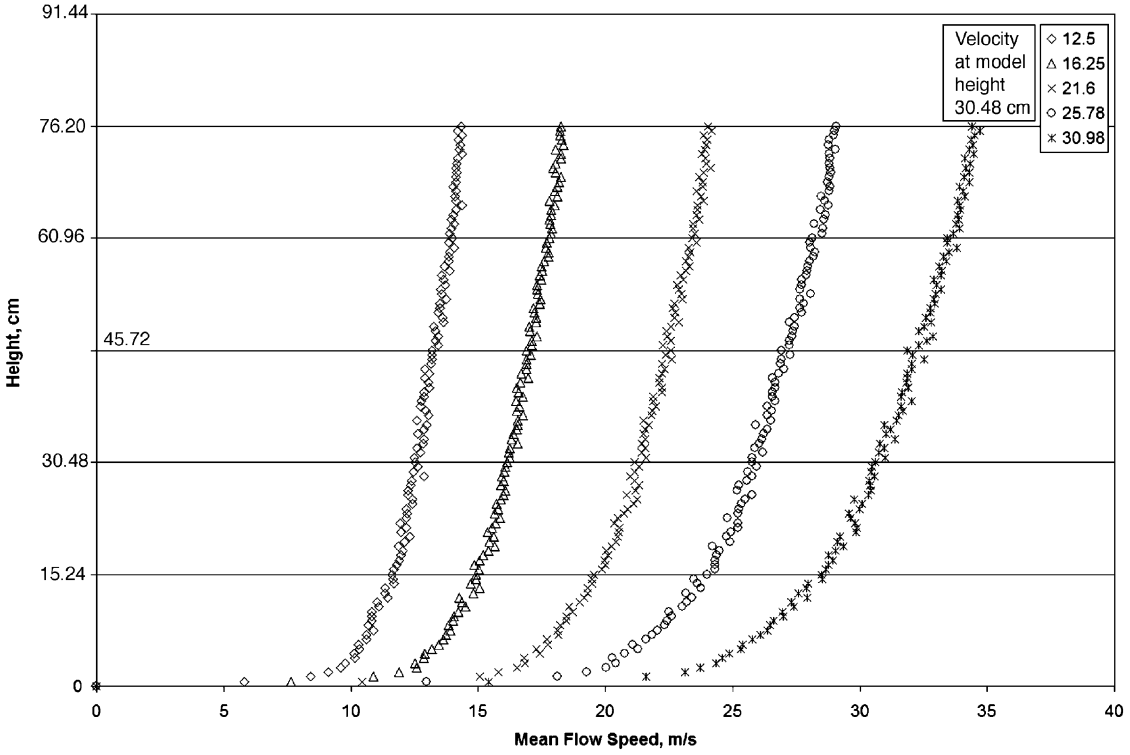

Fig. 8. Boundary layer profiles.

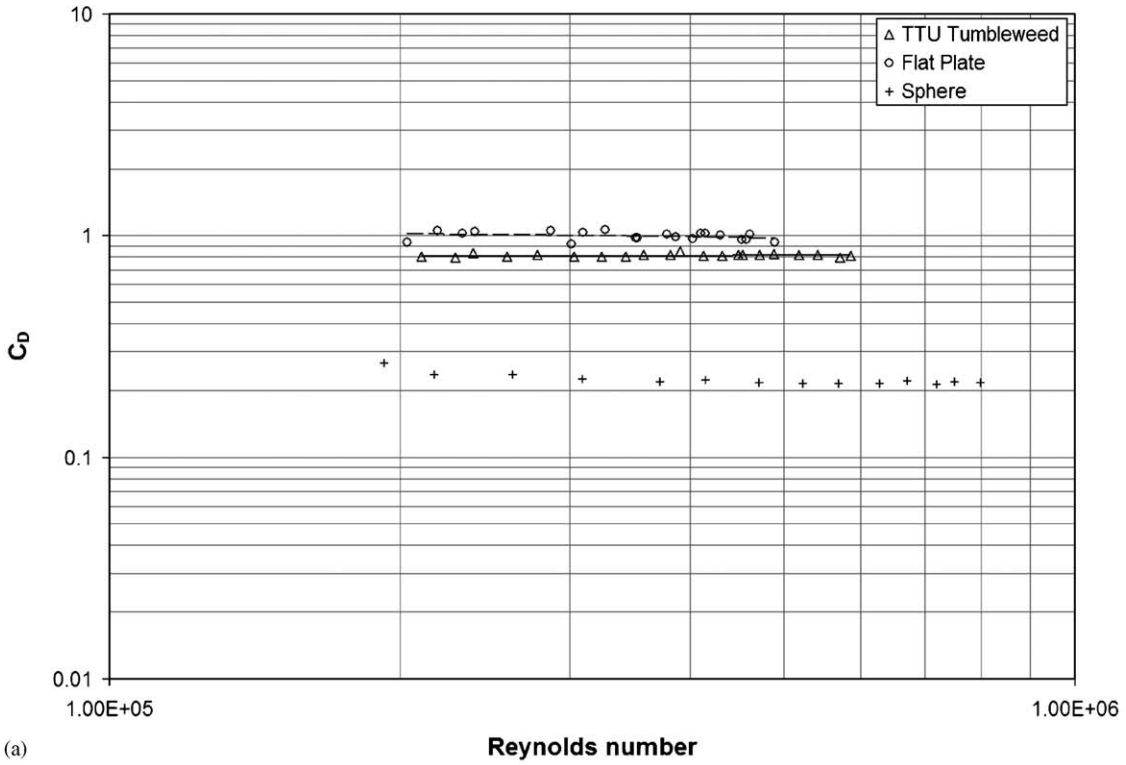

(a)

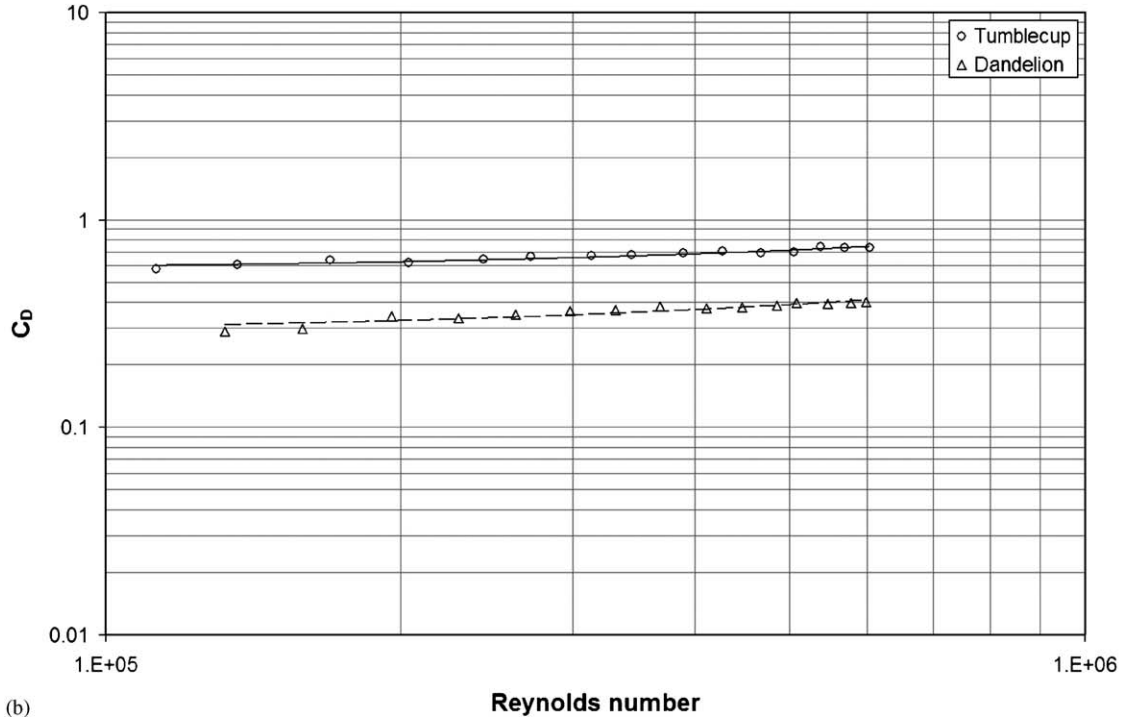

(b)

Fig. 9. C_D as a function of Re_D for all models in ABL section: (a) TTU tumbleweed, sphere, and flat plate; (b) LaRC models.

shown in Figs. 10 and 11(a), (b) for a mid-range Reynolds number (~500 000). The turbulence intensity profiles show the correct order, $I_u > I_v > I_w$, and the magnitudes decrease with height as they should. The intensities for the grid and fence only are of similar magnitude, but the intensities generated by the spires are noticeably smaller. At a height of 400 mm, the longitudinal or *u*-component of turbulent intensity is approximately 20% greater for the ABL generated using the fence/grid and fence only compared to the fence/spires. The turbulent intensities for the *v* and *w* components are also between 15% and 20% larger with the fence or grid compared to the spires.

The last evaluation of the ABLs generated is to calculate the integral length scale at model height for each of the three boundary layer profiles used in the turbulence intensity investigation described previously. Using Taylor's hypothesis, the integral time scale at model height is determined and, using the mean velocity, the integral length scale is calculated. The resulting length scales for each of the three profiles are larger than all model diameters. Cheng et al. (1992) reported that the mean drag of a square cylinder of diameter D is independent of turbulence length scale, L_u over the range $3.4 > L_u/D > 0.8$. This result is generally supported by other studies (Li and Melbourne, 1995; Laneville, 1973) using different bodies over a range L_u/l_c up to about 10, where l_c is the characteristic length of the body. Basically, the integral length scale represents the largest size scale of the energy containing eddies, and eddies of model size or larger affect the entire model and do not lose much energy as it passes the model; thus on average the mean drag force is not significantly affected. Note a fluctuating drag force was not obtained in this work, but it is accepted in building aerodynamics to use admittance functions that are functions of the turbulence frequencies and the body shape to calculate a fluctuating drag force [see e.g., Cermak (1976), Flay and Vickery (1995), Cheng et al. (1992)].

The drag coefficient for the TTU tumbleweed and the LaRC tumblecup and dandelion were tested over the full range of Reynolds numbers using ABL profiles generated using the grid and spires as described previously. The average C_D of the tumbleweed increased about 1.5% with the grid and decreased about 10% with the spires. The tumblecup drag coefficient showed an increase of 3.7% with the grid and a decrease of 6.1% with the spires. The dandelion drag coefficient showed an increase of 0.2% with the grid and a decrease of 10.5% with the spires. The resulting average drag coefficients for the tumbleweed and NASA models are summarized in Table 1. The results presented in the table are for zero degree orientation angles with all models. These results show that the drag coefficient of the TTU and LaRC tumbleweeds are affected by free-stream turbulence, much like that reported building aerodynamics, although its value is constant over the range of Reynolds numbers tested. The data suggests that the longitudinal turbulence intensity values affect the average C_D more than the transverse or vertical components, although a limited range of transverse and vertical intensities were used. To evaluate the transverse intensities in more detail would require a setup similar to what is reported in Cermak (1995) and was beyond the scope of this work.

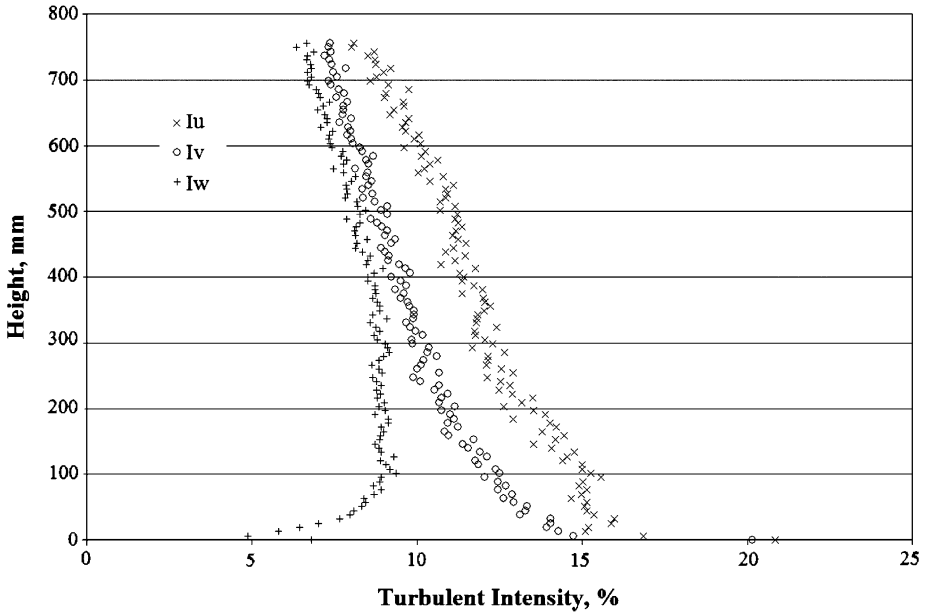

Fig. 10. Turbulence intensity profiles: fence and carpet only (baseline).

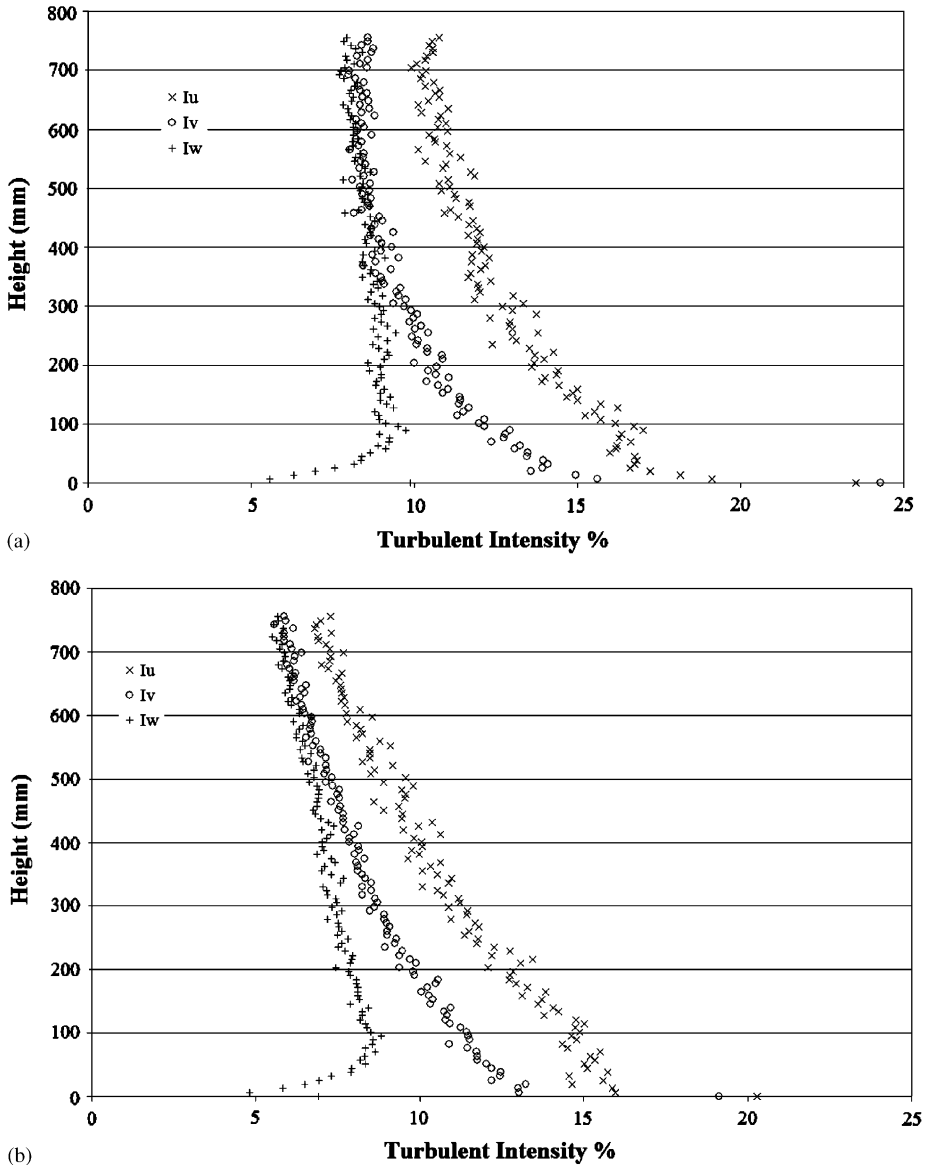

Fig. 11. Turbulence intensity profiles: (a) fence, carpet, and grid (referred to as grid); (b) fence, carpet, and spires (referred to as spires).

3.3. Drag-orientation results

For the drag-orientation testing, a fixed wind speed of ~20 m/s (at model height, 30.48 cm) was used throughout every orientation.[1] Three data points at each orientation were taken, each consisting of an average of 30 s of data. Since the data is comprised of the three orientation angles and a drag coefficient, it could not easily be viewed. The approach to analyzing the data was to map each set of angles and their respective drag coefficient to a point on the surface of a sphere with the radius of the tumbleweed. The merits of mapping C_D to the surface of a sphere will be demonstrated in the dynamic modelling section. Utilizing the symmetry of the model, the data was then mirrored on each symmetry plane to create data points around the full sphere. Once mapped to the sphere surface, a function, $C_D(x,y,z)$ was fitted

[1]The F/T sensor recorded six axes of data, the only data that would not average to zero over one complete roll of the ball was the drag component. However, the yaw moment combined with the side force could possibly assist the device to free itself if it were stuck against an obstacle.

Table 1
Summary of wind tunnel results for all concept models, average C_D

Test configuration	TTU tumbleweed	NASA tumblecup	NASA dandelion
Aerodynamic	0.93	0.72	0.40
ABL	0.68	0.68	0.37
ABL, grid	0.69	0.71	0.38
ABL, spires	0.61	0.64	0.34

to the data using a fourth-degree polynomial in x, y, and z. The function was created in this form in order to be directly inserted into the dynamic model presented in the next section.

Due to the limitations of the ball joint in the test set-up, two data points defining C_D on the extreme top and bottom of the model were entered into the data set prior to the function fitting. When the tumbleweed is viewed from the top or bottom, the surfaces that define the sectors of the tumbleweed are oriented parallel to wind in cross-flow, and the model profile looks essentially like a flat plate or circular area and therefore C_D at these points was set equal to that of a flat plate in cross-flow. Without the insertion of these points, C_D of the tumbleweed would be misrepresented by the function when evaluated at angles outside the test range.

To visualize the fitted function, points on the upper half of the sphere were projected onto the x–y plane in spherical coordinates, an r–θ plane with $\phi = 0$) and the C_D was plotted on the z-axis, as shown in Fig. 12. The solid points on the plot represent the actual data points obtained from the tests. A maximum error was calculated from the curve fit to the actual data to be roughly 5%, showing a fairly good fit of the data. From Fig. 12, it can be seen why the insertion of the points on the top and bottom of the tumbleweed were necessary. Without these points, this curve would most likely be of parabolic shape that would greatly underestimate C_D when the top or bottom of the model is oriented perpendicular to the wind.

4. Dynamic modelling

4.1. Kinematics

With the force function developed from the wind tunnel testing, the dynamic model of the rolling tumbleweed was then generated. The model presented here has been limited to rolling without slip and is not allowed to leave the surface, thus having three degrees of freedom in rotational motion with two translational components of motion defined by the rotations. Since all three rotation angles are allowed to evolve without bounds, commonly used Euler angle rotation sequences would not suffice; therefore the use of Euler parameters was chosen (Junkins and Turner, 1985; Greenwood, 2003; Corben and Stehle, 1950). Unlike the kinematic differential equations produced from Euler angle sequences that are nonlinear, transcendental, and contain singularities, the Euler parameters provide a universally nonsingular set of kinematic differential equations relating the parameters to the body angular velocity components (Junkins and Turner, 1985). The frames of reference used in the modelling are shown in Fig. 13.

The kinematic constraints on the translational motion due to the roll without slip condition were formulated by knowing that $v = R\omega$ for a rolling body with constant contact and no slip on a surface. If the scalar product of the body and the $\hat{n}_2$ component are then multiplied by the radius of the body, the result is the velocity in the $\hat{n}_1$ direction. Repeating this for the velocity in the $\hat{n}_2$ direction yields the following two differential equations that define the two components of translational motion $q_4(t)$ and $q_5(t)$:

$$\dot{q}_4(t) = R(x,\phi)\,{}^N\vec{\omega}^B \cdot \hat{n}_2,$$
$$\dot{q}_5(t) = R(x,\phi)\,{}^N\vec{\omega}^B \cdot \hat{n}_1. \tag{1}$$

By defining the translational motion in this way, the equations model a spheroid with radius $R(x,\phi)$ rolling on a flat surface.

4.2. Equations of motion

In order to capture both the forcing and hindering terms of the wind drag on the model, an expression for the relative velocity of the wind acting on the tumbleweed was constructed as

$$\vec{V}_{\text{rel}} = \vec{V}_{\text{wind}} - {}^o\vec{v}^{\text{cg}}, \tag{2}$$

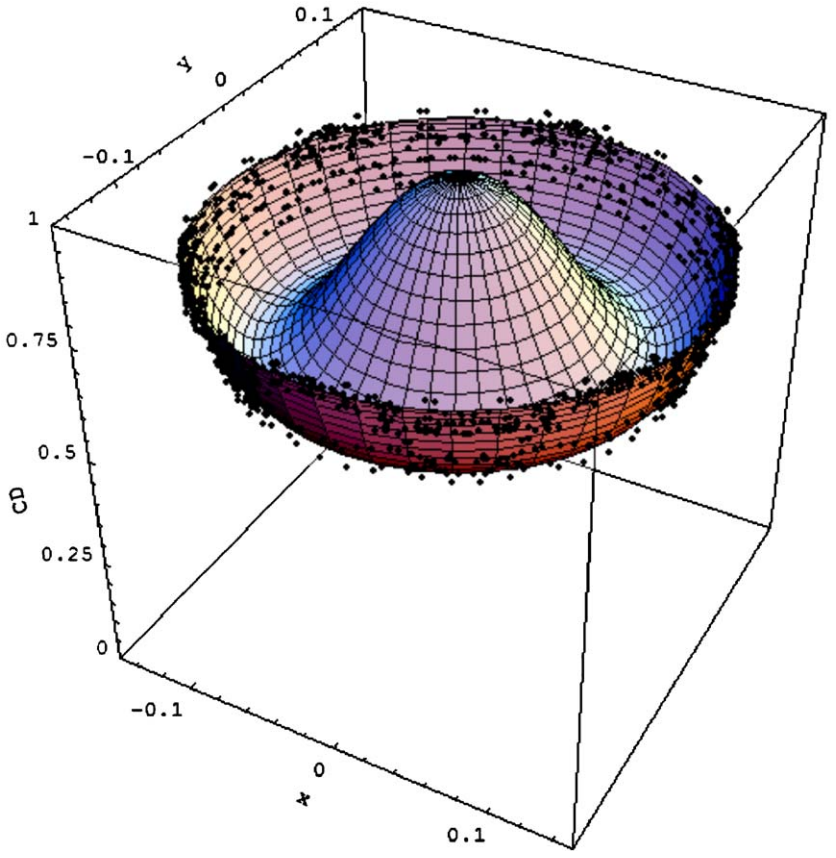

Fig. 12. C_D function obtained from wind tunnel testing.

From this, an expression for the drag force on the tumbleweed was developed using the drag coefficient as

$$F_D = C_D(x,y,z)\tfrac{1}{2}\rho A|\vec{V}_{\text{rel}}|^2\frac{\vec{V}_{\text{rel}}}{|\vec{V}_{\text{rel}}|} \tag{3}$$

or

$$F_D = C_D(x,y,z)\tfrac{1}{2}\rho A|\vec{V}_{\text{rel}}|\vec{V}_{\text{rel}}, \tag{4}$$

where

$$\begin{aligned} C_D(x,y,z) = {} & 0.323 + 3.38\times10^{-5}x + 22.3x^2 - 1.87\times10^{-3}x^3 + 3.35\times10^{-2}x^4 + 6.99\times10^{-12}y + 22.3y^2 \\ & + 3.99\times10^{-10}y^3 - 3.18\times10^{-2}y^4 + 5.26\times10^{-10}z - 19.6z^2 - 3.25\times10^{-8}z^3 + 2.06\times10^{3}z^4, \end{aligned} \tag{5}$$

as measured and described in Section 3.3. The terms x, y, and z in Eq. (5) are defined in Eq. (7). This C_D functional relationship maps the wind effects onto the tumbleweed for any orientation of the device relative to the prevailing wind vector, and allows the experimentally modelled fluid-structure interaction to drive our dynamic model described herein. Eq. (4) models the forcing effect of the wind when the velocity of the tumbleweed is less than the wind velocity and models the opposition to motion effect when the tumbleweed velocity is greater than the wind velocity (as in the case of when the tumbleweed rolls down an incline or rolls in still air). Expressions for the weight of the tumbleweed and for the damping effects due to rolling resistance were defined as

$$\begin{aligned} F_g &= -mg\hat{n}_3, \\ F_{rr} &= C_{rr}[-({}^o\bar{v}^{\text{cg}}\cdot\hat{n}_1)\hat{n}_1 - ({}^o\bar{v}^{\text{cg}}\cdot\hat{n}_2)\hat{n}_2], \end{aligned} \tag{6}$$

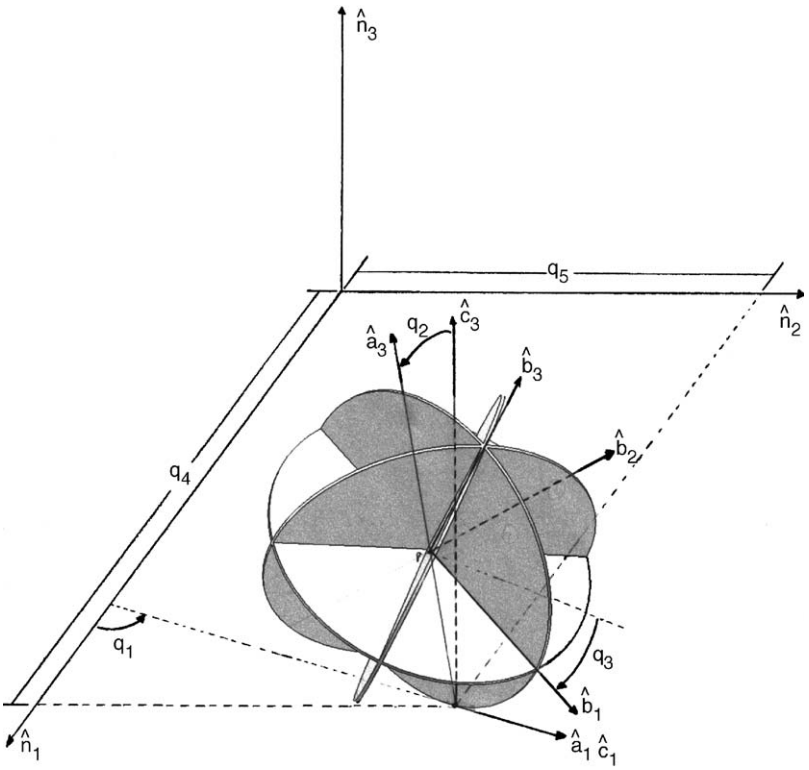

Fig. 13. Reference frames and angle definitions for the dynamic model.

where C_{rr} is a viscous coefficient of rolling resistance used to estimate the drag effects of the sharp-edged device rolling in loose soil.[2] The forces from Eqs. (4) and (6) were then summed to create the total nonconstraint force term for the tumbleweed model. At this point, an expression for the angular acceleration, ${}^N\vec{\alpha}^B$, was developed by simply taking the first time derivative of the angular velocity of the body.

The equations of motion for the tumbleweed model in terms of the Euler parameters and the three generalized angular speeds were derived using Kane's form of the Gibbs–Appell equations (Kane and Levinson, 1985) in symbolic form using *Mathematica* based tools (Barhorst, 1998). With the resulting three equations for the angular speeds, the four kinematic differential equations for the Euler parameters, and the kinematic constraint equations from Eq. (1), the motion of the tumbleweed is fully defined.

4.3. Models

Three simulation models were created with only slight variations. The first model (Model 1) was created with a simple spherical geometry and used the C_D function from Eq. (5). This model was used to facilitate the validation of the drag function, Eq. (5). A second model (Model 2) was then created with the kinematic geometry modelled as a variable radius spheroid to simulate the "bobbing" motion of the tumbleweed as it rolls and the forcing function was redefined with a constant C_D; this was used to verify the geometry function discussed in Section 4.3.2. The third model (Model 3) was then created by the "complete" model using this variable geometry and the variable C_D function, Eq. (5).

4.3.1. Drag map implementation

For the first and third models created for this study, it was necessary to implement the C_D mapping function developed from the wind tunnel testing. As discussed before, each set of orientation angles was mapped to a point on

[2]See Section 5.1.

the surface of a sphere with the same radius as the tumbleweed. A function was then fit to the data in the form $C_D(x, y, z)$ to describe the drag coefficient of the tumbleweed in any orientation relative to the wind. The true merit of choosing to map these points to the surface of a sphere comes from the simplicity of implementing the drag model into the dynamic model. The arguments x, y, and z are simply found as follows, and directly input into the $C_D(x, y, z)$ function as the dynamics evolve providing a new C_D at each time step

$$x = -R\left(\frac{\vec{V}_{\text{rel}}}{|\vec{V}_{\text{rel}}|}\right) \cdot \hat{b}_2,$$
$$y = -R\left(\frac{\vec{V}_{\text{rel}}}{|\vec{V}_{\text{rel}}|}\right) \cdot \hat{b}_1, \quad \text{and} \quad z = -R\left(\frac{\vec{V}_{\text{rel}}}{|\vec{V}_{\text{rel}}|}\right) \cdot \hat{b}_3. \tag{7}$$

4.3.2. Geometry implementation

Implementing the geometry of the tumbleweed first required that a closed-form function be developed that would define the radius of the tumbleweed. Since the TTU tumbleweed is not a trivial shape, the development of an expression to define its radius was not a simple task. Because of this complexity, for the function used to define the geometry in the model presented here it was assumed that the webbing material used in the tumbleweed construction is a cloth type material that cannot support the compressive load from the weight of the tumbleweed. This simplification requires that a hexagonal ovoid shape be modelled, which is a much simpler geometry. Fig. 14(a) shows the geometry model created to define the radius of the tumbleweed.

It must be noted that the geometry implemented into the models is not a true representation of the geometry of the tumbleweed. The model is only able to simulate the "bobbing" motion of the tumbleweed as it rolls and does not give the dynamic model the ability to predict the motion halting due to the tumbleweed falling into one of its removed sectors. Another geometry definition was created that is a single closed-form expression that defines the geometry of the tumbleweed. This expression was developed with the intentions of being used for the dynamic model presented here, but due to the complex switching algorithms that would be required to predict the true motion of the tumbleweed switching from disk to disk and having the possibility of multiple points in contact with the surface, it not implemented at this time. Fig. 14(b) shows the geometry defined by the complete expression.

4.3.3. Wind model

In order to create realistic wind condition in the dynamic model, experimentally obtained wind data from the Wind Science and Engineering Research Center at TTU was used. The data consisted of 15 min of full-scale wind speed and direction data sampled at a frequency of 30 Hz. The data was then broken down into the $\hat{n}_1$ and $\hat{n}_2$ components. The

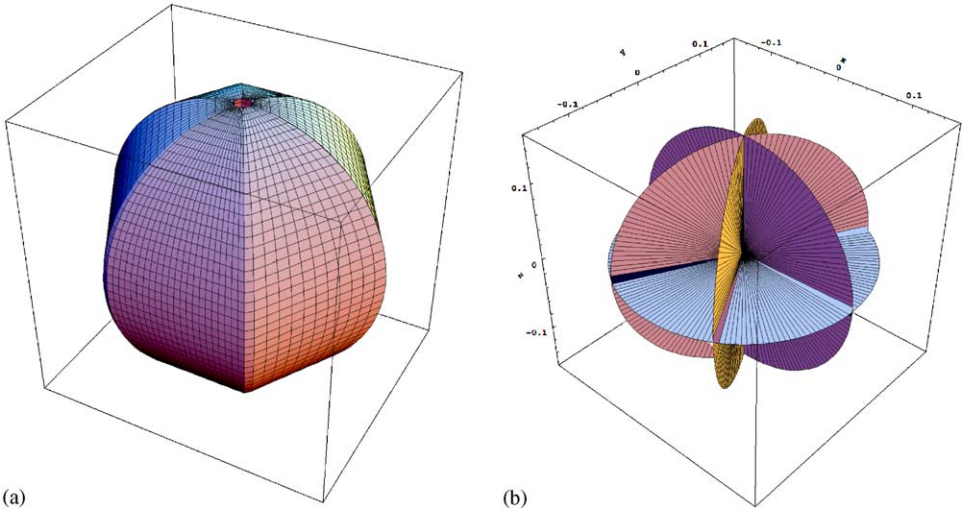

Fig. 14. Plots of the geometry expressions developed for the TTU tumbleweed: (a) simplified geometry used; (b) true geometry definition.

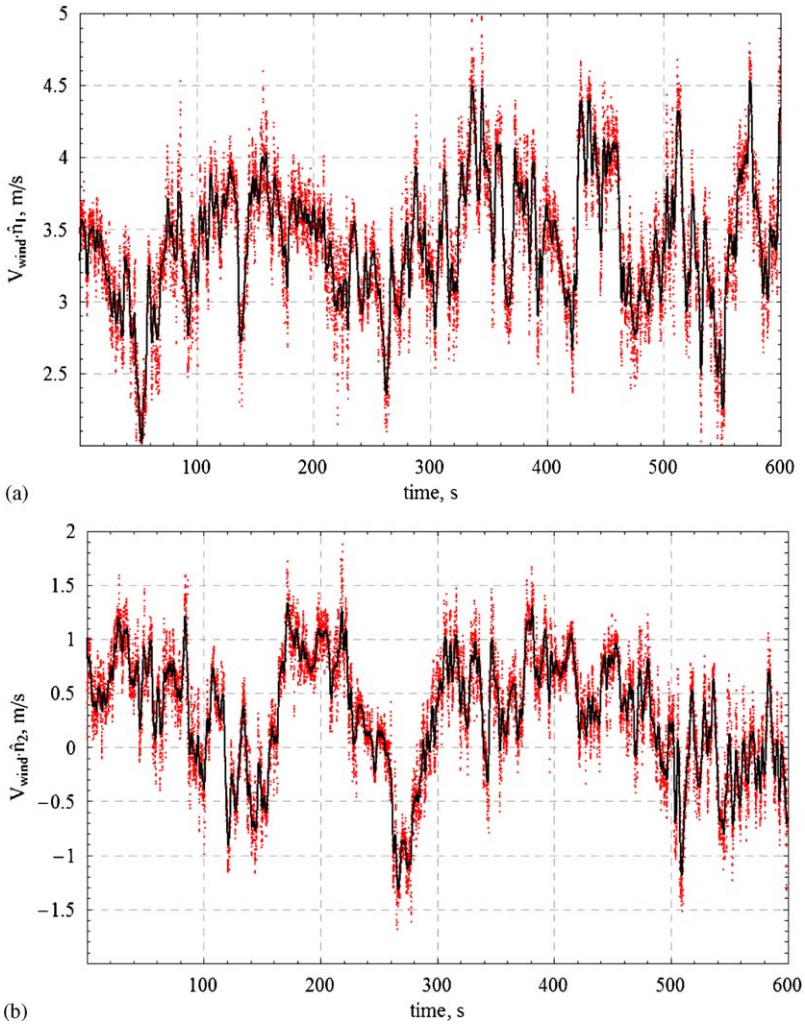

Fig. 15. Time history wind data: (a) $\hat{n}_1$ direction; (b) $\hat{n}_2$ direction.

data was filtered with a convolution filter routine created in *Mathematica* to smooth some of the noise in the data. With the data slightly smoothed, the mean magnitude of the wind velocity was then scaled to be 3.5 m/s at model height, which was taken from the literature (Lorenz, 1996) to be the most probable wind speed. Figs. 15(a), (b) shows the filtered (solid) and unfiltered (gray, red when viewed in color) data points for the $\hat{n}_1$ and $\hat{n}_2$ components of the wind model.

A check was then performed to investigate whether this data fit the probability distribution for wind speeds found on Mars. The data for windy conditions (Lorenz, 1996) was compared to a probability distribution created from the wind model obtained above. The two probability distributions are shown in Fig. 16. It can easily be seen that the data obtained does not fit the Martian wind speed distribution. However, since the wind model used is concentrated at the mean of the distribution of the published data, it creates a conservative approach to modelling of the Martian wind velocity distribution. The data used in this model does not have any high- or low-speed gusts like the data represented by the Weibull distribution in the figure. It should be noted that high-speed gusts will help the general mobility of these wind-driven sensor platform concepts. Not using the speeds on either end of the distribution is a conservative approach that avoids long periods of little motion at the expense of not having any periods of more rapid motion.

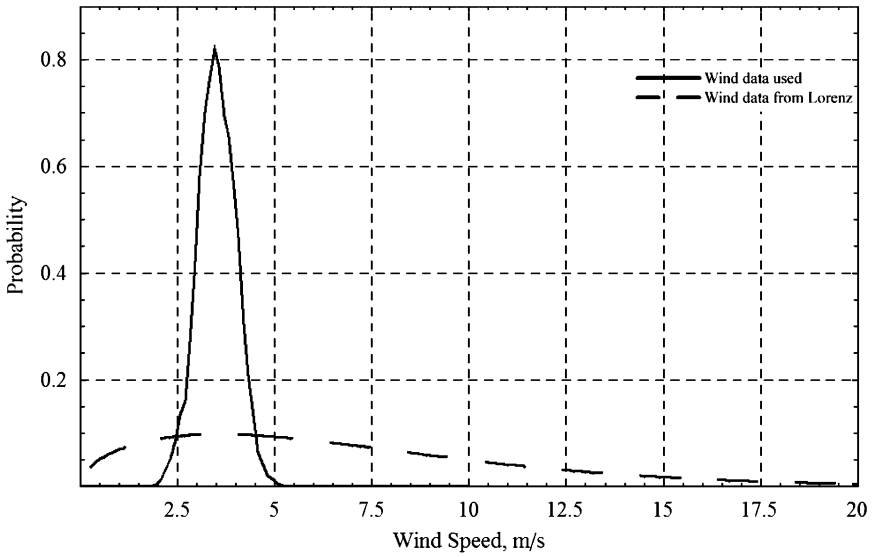

Fig. 16. Wind speed probability distributions.

5. Simulation results

5.1. Set-up

Three primary simulation cases were generated in this study. The first case (denoted as Case 1 hereafter) was chosen to represent the atmospheric properties and gravitational conditions found on earth to verify that the simulation provided realistic results. The second and third cases (denoted as Cases 2 and 3) were chosen to represent the surface conditions likely to be found on Mars. The atmospheric and gravitational properties for each case along with the physical properties of the tumbleweed and other physical parameters are summarized in Table 2. The gravitational and atmospheric properties were obtained from the literature (Antol et al., 2003; Williams, 2004).

The physical properties of the tumbleweed used in the first two cases were calculated using *AutoDesk Inventor* and are based on the tumbleweed being constructed from Polystone® UHMW Polyethylene. This material is chosen strictly for its density and provides a conservative estimate of the weight of the tumbleweed. For Case 3, the estimated physical properties of several prototypes that have been built using commonly found poster board and foam core presentation board were used. These prototypes typically weigh less than one-quarter of what was calculated using the UMHW density but, for simplicity, the weight was chosen to be exactly one-quarter of the weight used in the first two cases. For the forces from Eq. (6), an estimate for the rolling resistance coefficient in sandy dirt was used for Cases 1 and 2, while for Case 3 an estimate for rolling resistance in soft sand was used (Avalone and Baumeister III, 1987).

Prior to running any of the above-mentioned simulation cases, several very simple cases involving parameters typically found on Earth, and straight-line, constant velocity winds were run. These cases, along with Case 1, were used to verify several key issues pertinent to the verification of the simulation. Properties such as the terminal velocity of the tumbleweed being less than the wind velocity, and realistic acceleration and deceleration when the wind is turned on and off in the simulation were verified among many other rudimentary concepts.

For Case 1, a simple wind model was developed to test the functionality of the simulation and to verify that the results were realistic. This wind model, shown in Fig. 17, starts as a wind velocity vector in the $\hat{n}_1$ direction, then sweeps to a purely $\hat{n}_2$ velocity vector, and then sweeps back to the $\hat{n}_1$ direction and dissipates to a calm condition. Using this wind model forces the simulation to predict the effects of a changing wind and allows the tumbleweed to come to a halt after the wind stops. Forcing the simulation to predict these shifts in motion provides results that can be, in addition to the previously mentioned simplified cases, intuitively inspected to determine the validity of the model.

Table 2
Physical conditions and properties used in simulations

Property	Case 1	Case 2	Case 3
Gravity (m/s^2)	9.81	3.71	3.71
Atm. Density (kg/m^3)	1.2	0.0155	0.0155
Tumbleweed mass (kg)	0.853	0.853	0.213
I_{11} (kg m^2)	0.00685	0.00685	0.001713
I_{22} (kg m^2)	0.00686	0.00686	0.001715
I_{33} (kg m^2)	0.00624	0.00624	0.00156
Rolling resistance, C_{rr}	0.3	0.3	0.1
Simulation time (s)	40	600	600

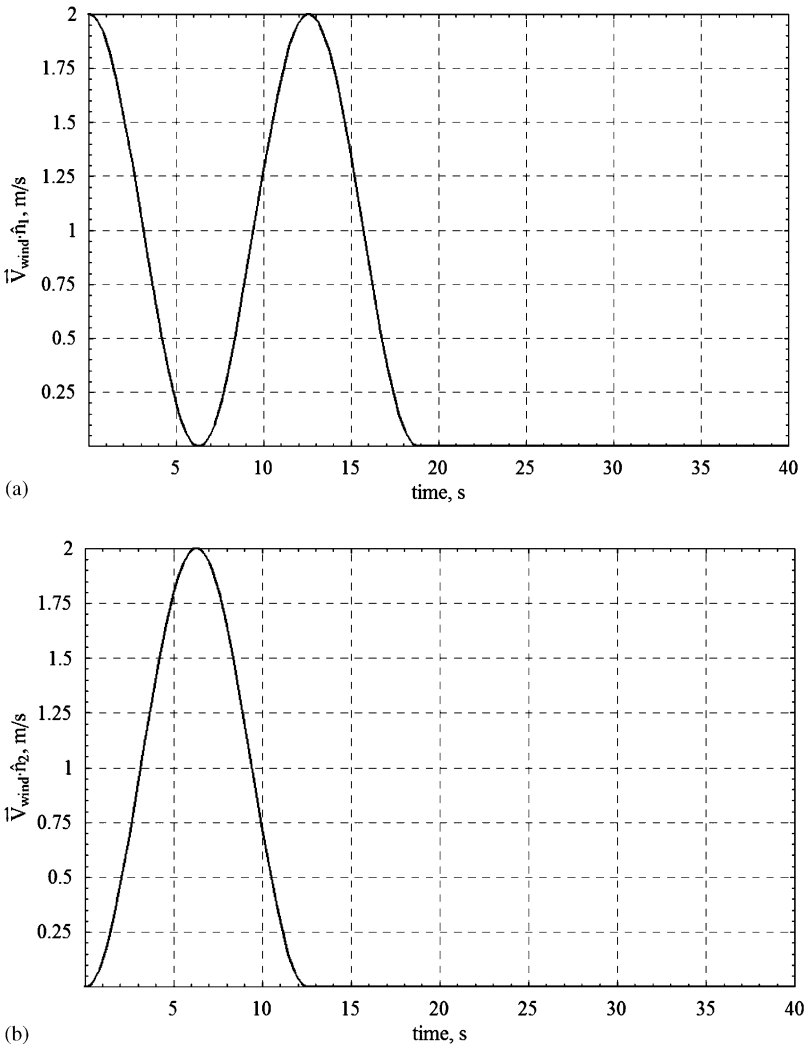

Fig. 17. Vector components of the wind velocity for case 1: (a) $\hat{n}_1$ direction; (b) $\hat{n}_2$ direction.

5.2. Results

For the first simulation case, a plot of the path of the point of contact with wind velocity vectors superimposed was generated to ensure that the dynamic behavior of the rolling body fit what was intuitively expected. This plot, shown in Fig. 18, matches the expectations of the wind's effects on the motion of the tumbleweed. As further verification, animations of the device were created to ascertain the reasonableness of the model. Shown in Fig. 19 are snapshots at 2 s intervals; the wind vector is drawn as well and is shown on the vertical axis of the reference frame. The model reacts as expected.

For Cases 2 and 3, the simulation was run using the geometry of Model 3 only. The wind model presented in the previous section was used with Martian atmospheric and gravitational properties. The simulations were run for 10 min and utilized the same initial conditions used in Case 1. The path of the contact point in the plane of motion was then plotted as in the previous case, but without velocity vectors, and is shown in Fig. 20.

It is easily seen when comparing the results from Cases 2 and 3 that even with the increased rolling resistance, the lighter weight has a dominating effect on the dynamics. The reduced weight model rolls roughly three times further in the same conditions. However, the very slow motion of the tumbleweed raises the question of mobility on inclined surfaces. Several simulations were run using the parameters from Case 3, but with the addition of an inclined surface; wind vectors stayed in the base plane. It was found that the tumbleweed was unable to roll up even the slightest of inclines ($\sim 1^\circ$); so, basic calculations were performed to investigate the tumbleweed's mobility on inclinations. After performing these calculations, additional simulations were run to verify that the simulations and simplified calculations were in agreement. It should be noted that lift and rolling moments induced by the wind were not included in this simulation model. The tumbleweeds were always started from rest.

5.2.1. Hill climbing analysis

All of the results presented thus far have been generated for the tumbleweed rolling on a level surface. Simulations were run with various slope angles and it was found that the tumbleweed was undersized or overweight to climb even the smallest of hills when started from rest. In light of this, some brief calculations were performed to find the size requirements for various angles of inclination using the inequality presented in Eq. (8). These calculations are vastly simplified, equating the drag and gravitational forces. Using these simplified force calculations provides an estimate of the conditions for rolling, assuming no initial momentum, no lift, and no wind-induced rolling moments. Under these assumptions, we have

$$C_D \tfrac{1}{2} \rho_{\text{atm}} A V^2 \geqslant mg \sin\theta. \tag{8}$$

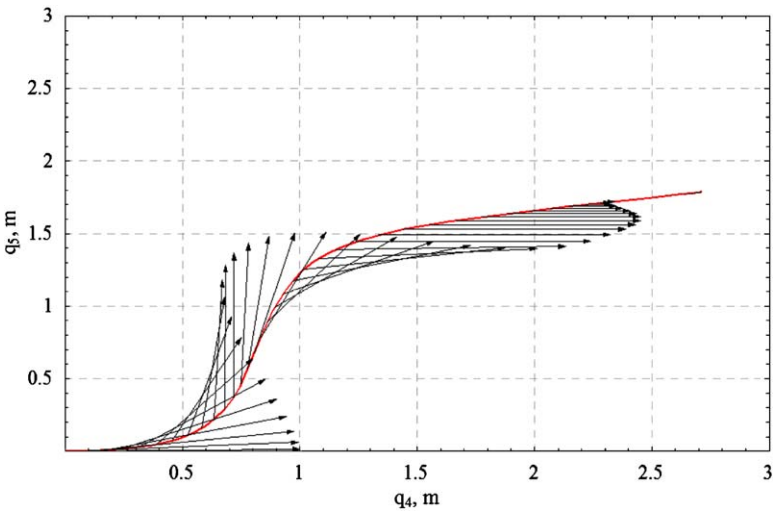

Fig. 18. Path of contact point with wind velocity vectors (case 1, model 1).

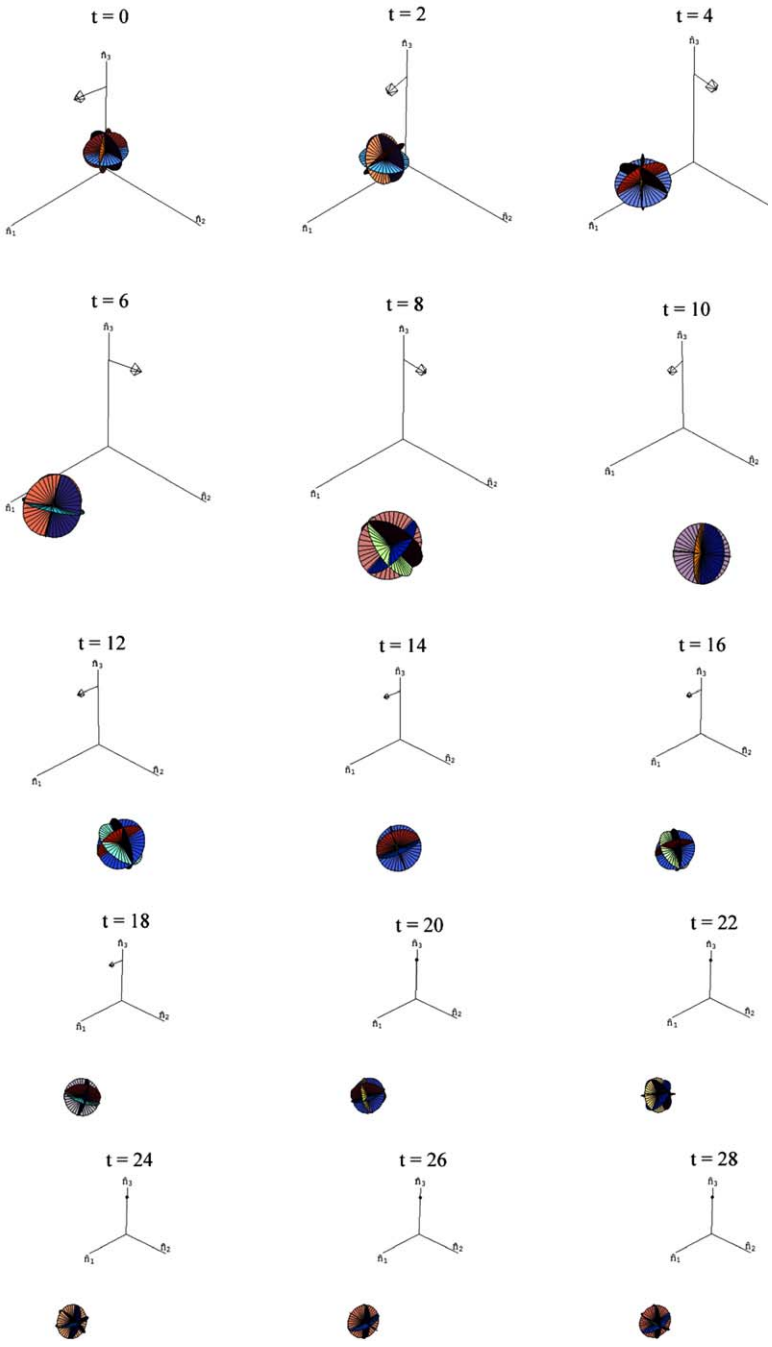

Fig. 19. Tumbleweed animation snapshots with wind vector.

Using an average C_D of 0.75 and an average wind speed of 3.5 m/s, the equation was rearranged as

$$\frac{R^2}{m} \geqslant 16.5854 \sin \theta. \tag{9}$$

The mass of the tumbleweed can be expressed in the following approximate form:

$$m \approx 4\pi R^2 t \rho, \tag{10}$$

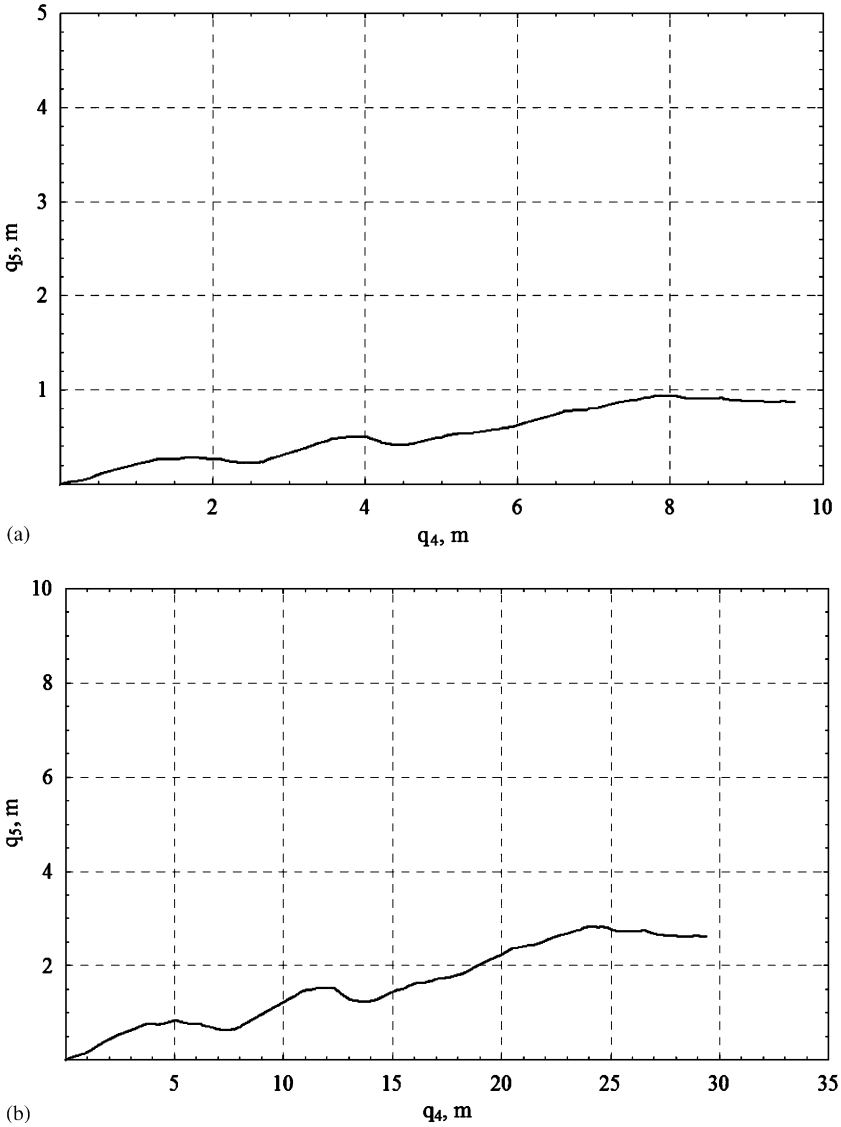

Fig. 20. Path of contact point: (a) Case (2); Case (3).

where t is the thickness of each disk [see Fig. 14(b)] and ρ is the density of the material used. Using this relationship for the mass of the tumbleweed in Eq. (9) results in the following equation, relating the disk thickness and material density to the angle of inclination

$$\frac{1}{\rho t} \geqslant 208.418 \sin \theta. \tag{11}$$

Using Eq. (11) along with the material density used in Case 3, a table of maximum disk thickness values for various angles of inclination was constructed and is presented in Table 3.

With the current disk thickness of roughly 3 mm, it is evident from Table 3 that an even lighter material would be required for the tumbleweed to have the ability to travel, starting from rest, over any significant incline.

Table 3
Maximum disk thickness for various inclination angles

Angle (°)	Equivalent grade (%)	Maximum thickness (mm)
0.573	1	2.065
1.146	2	1.033
1.718	3	0.689
2.291	4	0.517
2.862	5	0.414

6. Conclusions

In this study, we developed a wind tunnel model of the Martian atmospheric boundary layer in the TTU wind tunnel. This model was then used to measure drag characteristics of two NASA LaRC tumbleweed concepts as well as the TTU tumbleweed concept. The drag coefficient of all models tested were Reynolds number independent, although some dependence on free-stream longitudinal turbulence intensity existed. Utilizing angle of attack drag information measured relative to the TTU tumbleweed, we developed a dynamic simulation of the simplified rolling motion under realistic wind profiles for Mars. The work shows that the small TTU concept does roll in the wind but has trouble climbing obstacles with its current size/mass characteristics. We note that this simulation model did not include lift and wind-induced rolling moments which, if included, may bolster the mobility of TTU tumbleweed concept. Lighter materials will probably be required for the much smaller TTU concept to be viable.

Acknowledgments

This work was supported by grants from NASA Langley Research Center, Order number L-71124D, and the Texas Space Grant Consortium, Subcontract number UTA03-170 from prime NASA Grant number NGT5-40083.

References

Antol, J., Calhoun, P., Flick, J., Hajos, G., 2003. Low cost Mars surface exploration: the Mars tumbleweed. Technical Report, NASA Langley Research Center.

Avalone, E.A., Baumeister III, T. (Eds.), 1987. Marks' Standard Handbook for Mechanical Engineers, ninth ed. McGraw-Hill, New York.

Barhorst, A.A., 1998. Symbolic equation processing utilizing vector/dyad notation. Journal of Sound and Vibration 208 (5), 823–839.

Cermak, J., 1976. Aerodynamics of buildings. Annual Review of Fluid Mechanics 8, 75–106.

Cermak, J., 1995. Wind tunnel modelling of the atmospheric surface layer. Journal of Wind Engineering and Industrial Aerodynamics 54/55, 505–513.

Cheng, C., Lu, P., Chen, R., 1992. Wind loads on square cylinders in homogeneous turbulent flows. Journal of Wind Engineering and Industrial Aerodynamics 41–44, 739–749.

Corben, H.C., Stehle, P., 1950. Classical Mechanics. Wiley, New York.

Flay, R., Vickery, B., 1995. Pressure correlations on a rough cone in turbulent shear flow. Journal of Wind Engineering and Industrial Aerodynamics 58, 1–18.

Greenwood, D.T., 2003. Advanced Dynamics. Cambridge University Press, Cambridge, UK.

Hoerner, S.F., 1965. Fluid Dynamic Drag. Hoerner Fluid Dynamics, Bakers-field, CA.

Junkins, J.L., Turner, J.D., 1985. Optimal Spacecraft Rotational Maneuvers. Studies in Astronautics, vol. 3. Elsevier Scientific, New York.

Justus, C.G., Johnson, D.L., 2001. Mars global reference atmospheric model 2001 version (Mars-GRAM 2001) users guide. Technical Report, NASA/TM-2001-210961.

Kane, T.R., Levinson, D.A., 1985. Dynamics: Theory and Applications. McGraw-Hill, New York.

Kline, S.J., McClintock, F.A., 1953. Describing uncertainties in single-sample experiments. Mechanical Engineering 3.

Laneville, A., 1973. Effects of turbulence on wind induced vibrations of bluff bodies. Ph.D. Thesis, University of British Columbia, Vancouver, Canada.

Lee, B., 1976. Some effect of turbulence scale on the mean forces on a bluff body. Journal of Wind Engineering and Industrial Aerodynamics 1 (4), 361–370.

Li, Q., Melbourne, W., 1995. An experimental investigation of the effects of free-stream turbulence on streamwise surface pressures in separated and reattached flows. Journal of Wind Engineering and Industrial Aerodynamics 54/55, 313–323.

Lorenz, R.D., 1996. Martian surface wind speeds described by the Weibull distribution. Journal of Spacecraft and Rockets 33 (5), 754–756.

NASA, 2004. NASA's Mars Exploration Program, http://mars.jpl.nasa.gov/missions, Accessed 6/21/04.

Schlichting, H., 1979. Boundary-Layer Theory, seventh ed. Wiley, New York.

Williams, D.R., 2004. Mars Fact Sheet (online), NASA NSSDC website, http://nssdc.gsfc.nasa.gov/planetary/factsheet/marsfact.html, Accessed 6/21/04.